ECS Transactions

(Invited) CMOS-MEMS Based Microgravity Sensor and Its Application

To cite this article: Kazuya Masu *et al* 2020 *ECS Trans.* **97** 91

ECS Transactions, 97 (5) 91-108 (2020)
10.1149/09705.0091ecst ©The Electrochemical Society

CMOS-MEMS Microgravity Sensors and Their Application

K. Masu, K. Machida, D. Yamane, H. Ito, N. Ishihara,
T. M. Chang, M. Sone, R. Shigeyama, T. Ogata, and Y. Miyake

Tokyo Institute of Technology
4259 Nagatsuta, Midori-ku, Yokohama, Kanagawa 226-8503, Japan

This paper reviews the feature of newly developed CMOS-MEMS (microelectromechanical systems) and MEMS accelerometers and its application for a diagnosis of Parkinson's disease. In order to realize micro-G ($1G=9.8m/s^2$) level sensing, we propose and develop capacitive MEMS accelerometers with Au proof mass using the multi-layer metal technology. In order to reduce Brownian noise (B_N), which determines the sensitivity of MEMS accelerometer, we utilize Au as a high density proof mass. In addition, we investigate the crystal structure of Au in terms of the device reliability. Furthermore, we demonstrate the validity of applying the MEMS accelerometer for the early-stage diagnosis of Parkinson's disease. The experimental results regarding the sensor, the material and the diagnosis suggest that our microgravity sensor can pave the new way for the early-stage diagnosis of Parkinson's disease.

Introduction

MEMS (microelectromechanical systems) accelerometers are now widely used for a variety of applications in automotive, industrial, healthcare, entertainment, consumer handheld electronics, and so on (1, 2). The technical progress such as IoT (Internet of Thing) and AI demands the micro-G ($1G=9.8m/s^2$) level sensing with small sensor size (3, 4). In order to realize the micro-G level sensing, MEMS accelerometers with high sensitivity have to be developed. The sensitivity of the MEMS accelerometer depends on the Brownian noise (B_N), which is inversely proportional to the mass of the proof mass (5-8). In conventional silicon MEMS accelerometers, there are many reported techniques using bulk-micromachining and/or wafer bonding (9-17). MEMS accelerometers developed by bulk micromachined technology have B_{N} below 1 μG/√Hz and become quite large sensor module (6, 7, 13, 14). B_{N} of MEMS accelerometer fabricated by surface micromachined technology cannot exhibit the lower value than 10μG/√Hz (18-20). In order to realize the high sensitivity, we have proposed capacitive MEMS accelerometers with high-density proof mass and have been developing CMOS-MEMS and MEMS accelerometers (21-24) using a post-CMOS process compatible to CMOS LSI process (25).

From the viewpoint of the usage of gold material for MEMS structures, we have analyzed Au crystal structure to ensure the device reliability. It is revealed that the electroplated Au material has a potential of the material strength. Furthermore, we have developed diagnosis of Parkinson's disease as the application of the high sensitivity MEMS accelerometer. So far, walking trajectory and postural abnormality of Parkinson's disease patients and healthy persons are analyzed based on machine learning technique.

In this paper, we first present our recent research progress of high sensitivity MEMS and CMOS-MEMS accelerometers. Next, we show the results of the crystal structure analysis to the electroplated Au. Lastly, an application of the MEMS accelerometer is discussed in terms of early-stage diagnosis of Parkinson's disease.

MEMS Accelerometer for Micro-G Level Lensing

This chapter describes the design concept and fabrication results of the proposed MEMS accelerometer for micro-G level sensing.

Design concept

Figure 1 shows a schematic view of typical CMOS-MEMS and MEMS accelerometers (21-24). The MEMS accelerometer consists of suspensions, stoppers, a proof mass as upper electrode, and a fixed electrode. When the upper electrode is moving to the vertical direction by the input of acceleration, the capacitance is detected by the fixed electrode. The stoppers are built to prevent mechanical destruction caused by over-swinging of the upper electrode. The Brownian noise B_N is given by

$$B_N = \frac{\sqrt{4k_B T b}}{m} \;, \qquad [1]$$

where k_B, T, b and m are the Boltzmann constant (1.38×10^{-23} J/K), the absolute temperature, the viscous damping coefficient, and the proof mass of an accelerometer, respectively (21). As shown in eq. [1], B_N is inversely proportional to the proof mass. Thus, the conventional Si MEMS capacitive accelerometers result in a large-sized Si proof-mass when a low B_N is

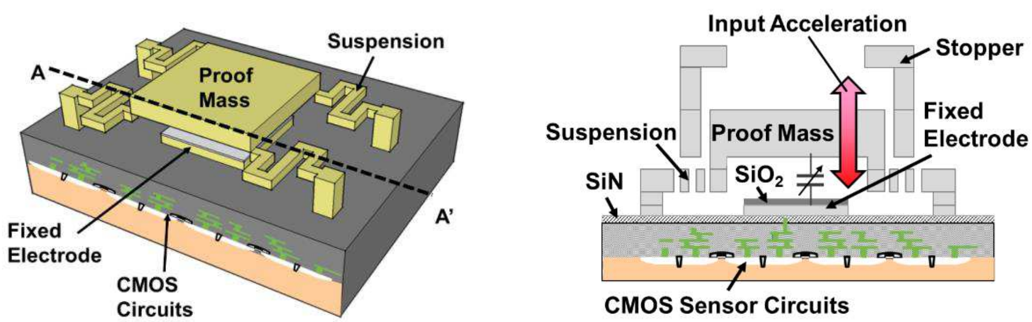

(a) (b)

Figure 1. A schematic view of CMOS-MEMS accelerometer(a) and (b).

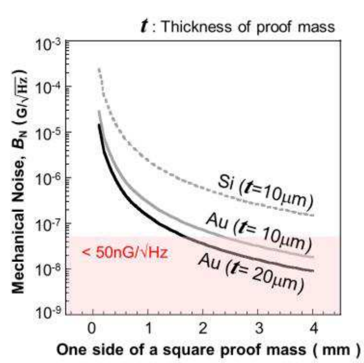

Figure 2. Mechanical noise analysis results.

obtained. Here, the density of Au (19.3×10^3 kg/m^3 at 298K) (26) is nearly an order of magnitude higher than that of Si (2.33×10^3 kg/m^3 at298K) (27). Utilizing gold material as a proof mass can achieve lower B_N compared to Si proof mass of the same size. For micro-G level sensing, the target resolution was determined to be below 50nG√Hz. Figure 2 shows analysis results of B_N as a function of the proof-mass size, where T and b are set to be 298K and 1.85×10^{-5} N・s/m, respectively. The thickness of the Si proof mass is set to be 10µm as the maximum thickness used for fabricating surface-micromachined MEMS accelerometers (27-29). We have developed gold proof mass structures with the thickness upwards of 12µm (22). On the other hand, we have to consider the structure of the proof mass comprising of the etching hole for removing the sacrificial film. Thus, the proof mass thickness will be designed by that of over 10µm. As the thickness of a single gold layer in the multi-layer technology was thinner than 20µm, we proposed to utilize multiple gold layers for the proof mass. The proof-mass structure with the thickness of 20µm can be achieved by using two gold layers in the multi-layer metal technology.

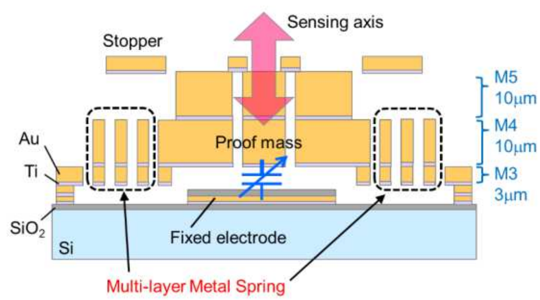

Figure 3. Schematic image of the proposed single-axis MEMS capacitive accelerometer.

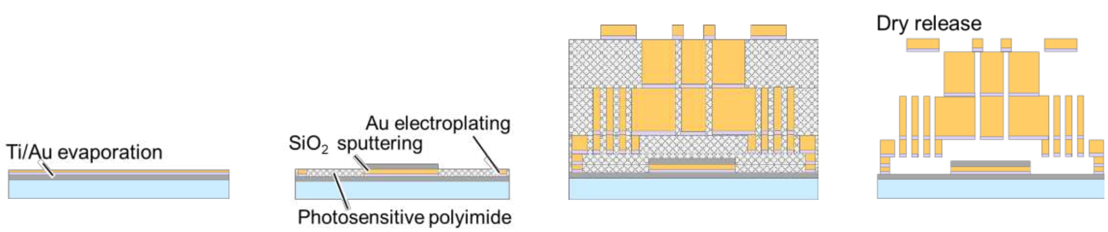

(a) (b) (c) (d)

Figure 4. Process flow. (a) Seed layer deposition, (b) M1 and SiO_2 layers patterning, (c) M2-M6 patterning, and (d) sacrificial layer etching.

Device fabrication

Figure 3 shows a schematic image of the proposed single-axis MEMS capacitive accelerometer. We utilize the third (M3) and the fourth (M4) layers for the spring structure, and M4 and the fifth (M5) layers for the proof mass. Figure 4 describes the device fabrication process flow. Firstly, Ti/Au seed layers were deposited by evaporation on a thermal-SiO_2 as shown in Fig. 4 (a). Gold electroplating process was then used to increase the thickness of the first Gold layer (M1). Photosensitive polyimide as a sacrificial layer was spin-coated and annealed at the temperature of 310 °C. An SiO_2 layer with a thickness of 1μm was deposited by sputtering (Fig. 4(b)). With the same Au pattering as for M1 layer, we made another five Au layers (M2-M6), as illustrated in Fig. 4(c). Finally, all the sacrificial layers were removed by O_2 plasma etching (Fig. 4 (d)).

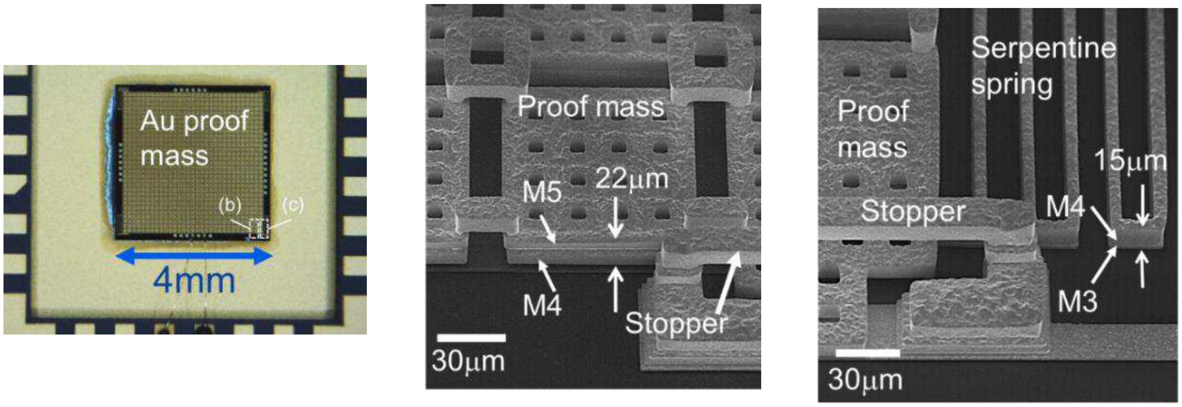

(a) (b) (c)

Figure 5. Fabricated device. (a) Chip view, (b) proof mass and (c) spring structure.

Figure 5 (a) is a chip view of the developed MEMS accelerometer. A gold proof mass was fabricated on a silicon substrate with the footprint of 4mm×4mm. The SEM micrograph of the proof mass is shown in Fig. 5(b). The gold proof-mass structure with the thickness of 22μm was successfully developed by employing M4 and M5 layers. Figure 5 (c) shows the SEM image of the serpentine spring structure made of M3 and M4 layers. Stopper structures were made of M6 layer and set above the proof mass. The serpentine springs and the stoppers were placed at each corner of the proof mass.

Experimental results and discussion

Acceleration responses. We measured capacitance between the proof mass and the fixed electrode when Z-axis acceleration was applied to the device as shown in Fig. 6.

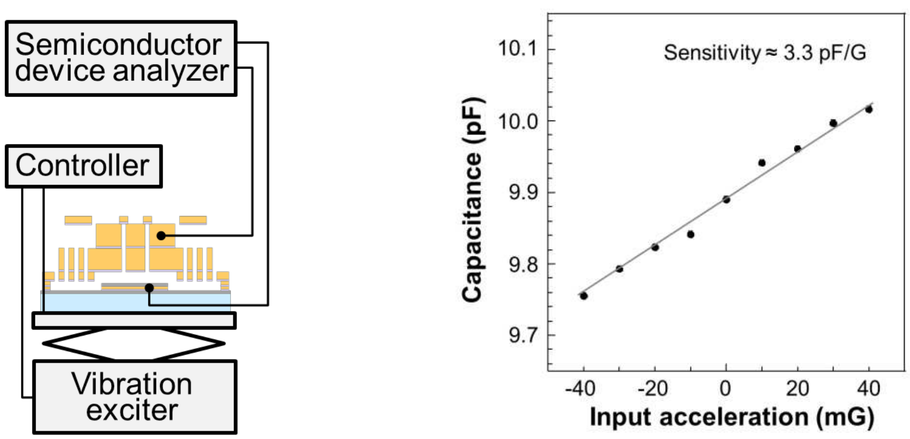

(a) (b)

Figure 6. Measured capacitance as a function of input acceleration. (a) Experimental setup and (b) measurement results.

Figure 6 (a) is the experimental setup, where the packaged MEMS device was set on a custom-designed printed circuit board (PCB) on a vibration exciter (WaveMaker05, Asahi Seisakusho) with the minimum input-acceleration step of 0.01G. A semiconductor device analyzer (B1500A, Agilent Tech., Inc.) was used to supply the DC bias voltage of 0.5V and measure the capacitance change with a ±0.1-V sinusoidal voltage at the frequency of 300kHz. Figure 6(b) shows the measured capacitance as a function of input acceleration at the frequency of 49.9Hz. The sensitivity was experimentally obtained to be 3.3pF/G.

Frequency characteristics. For the evaluation of mechanical characteristics and B_N, we measured the frequency responses of the fabricated MEMS device. Figure 7(a) shows the experimental setup with an LCR meter (IM3533-01, HIOKI E.E. Corp.). As shown in Fig. 7(b), the resonant frequency of the device was found to be 202Hz with the DC bias voltage of 0.5 V. To evaluate the B_N of the device, the following relationship (21) was used:

$$B_N = \sqrt{\frac{4k_B T\omega_r}{mQ}} \quad , \qquad [2]$$

where ω_r and Q are the resonant angular frequency and the quality factor, respectively. Table 1 summarizes the design and measured characteristics of the device, and the actual B_N was obtained to be 22nG/√Hz. Figure 8 compares B_N against the capacitance sensitivity with conventional MEMS accelerometers. Owing to the high density of gold, the B_N of this work was more than an order of magnitude lower than those of conventional when compared with the same sensitivity performance.

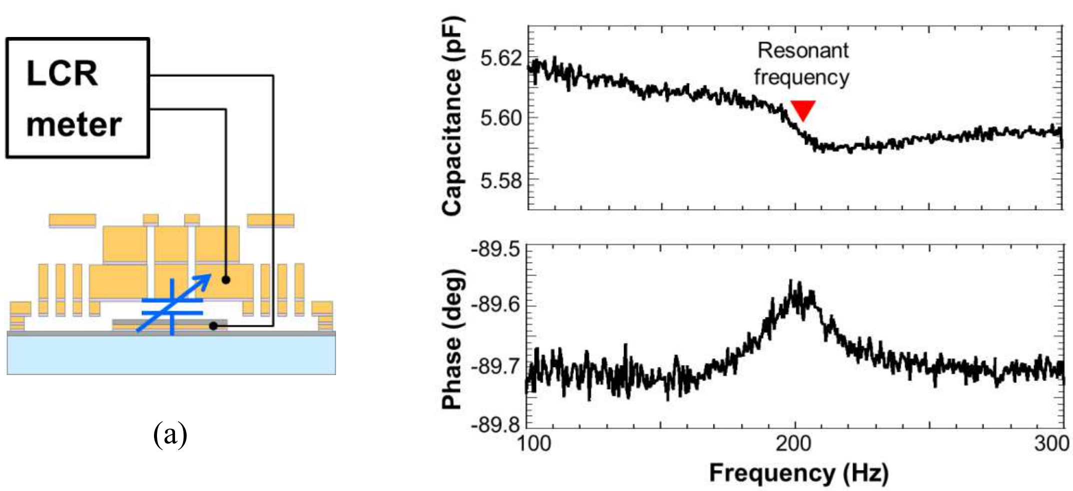

(a)

(b)

Figure 7. Measured capacitance and phase as a function of frequency. (a) Experimental setup and (b) measurement results.

Table 1 Summary of device characteristics.

	Design	Measured	Unit
m	3.28×10^{-6}	3.62×10^{-6}	kg
f_{res}	260	202	Hz
Q	289	131	
B_N	17	22	nG/√Hz

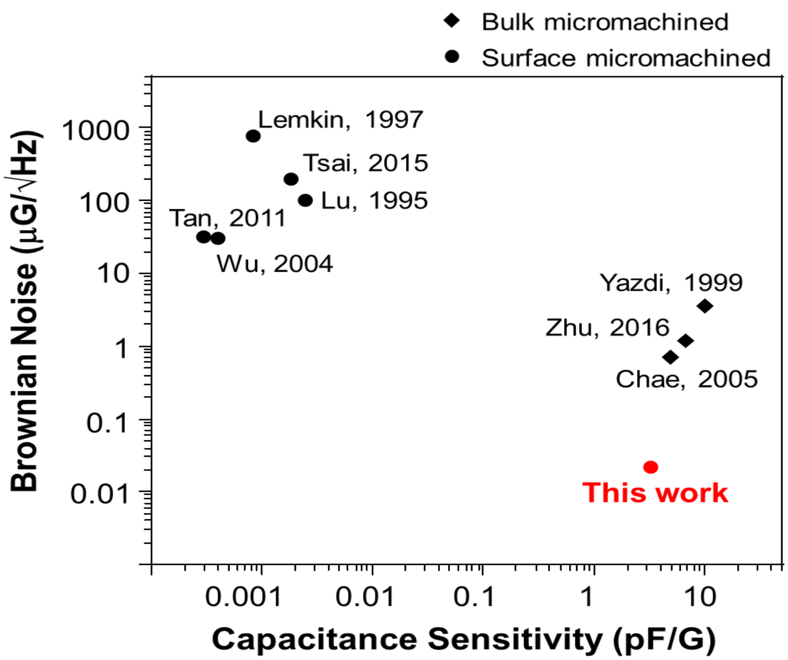

Figure 8. Comparison of B_N versus capacitance sensitivity (8,9,17-19,30-32).

The material strength analysis of the electroplated Au

This chapter describes the material strength analysis based on the micro-mechanical property anisotropy of the electroplated Au film.

Experimental

The Au film was electroplated using a cyanide-based electrolyte (33). The Au film was electroplated on a Pt substrate. For the micro-compression test, two Au micro-pillars were fabricated by focused ion beam (FIB, Hitachi: FB2100). Details of the electroplating and the FIB fabrication are reported in a previous study (33). Dimensions of the Au pillar were $10 \times 10 \times 20 \mu m^3$ with a square cross-section, and the long-side was either perpendicular (pillar 1, Fig. 9(a)) or parallel (pillar 2, Fig. 9(b)) to growth direction of the Au film.

The compression test was conducted using a test machine specially designed for micro-sized specimens equipped with a flat-ended diamond indenter at a constant displacement of 0.1μm/s controlled by a piezo-electric actuator. The load resolution was 10μN.

Crystal structure of the Au film was evaluated by an X-ray diffractometer (XRD, Ultima IV, Rigaku), a scanning electron microscope (SEM, S-4300SE, Hitachi) equipped with electron back scatter diffraction (EBSD) function, and transmission electron microscopy (TEM, 200kV, JEM2100, JEOL). Deformation behavior of the specimens was observed by a scanning ion microscope (SIM) equipped in the FIB.

Results and Discussion

Microstructures of the Au micro-pillars before and after the micro-compression test are shown in Figs. 9(c) to (f). Columnar texture-like microstructures having the long-axis perpendicular to the long-side of pillar 1 were observed. The long-axis of the micro-columnar textures were parallel to the long-side of pillar 2.

After the compression test, brittle fracture along the texture boundary was observed in

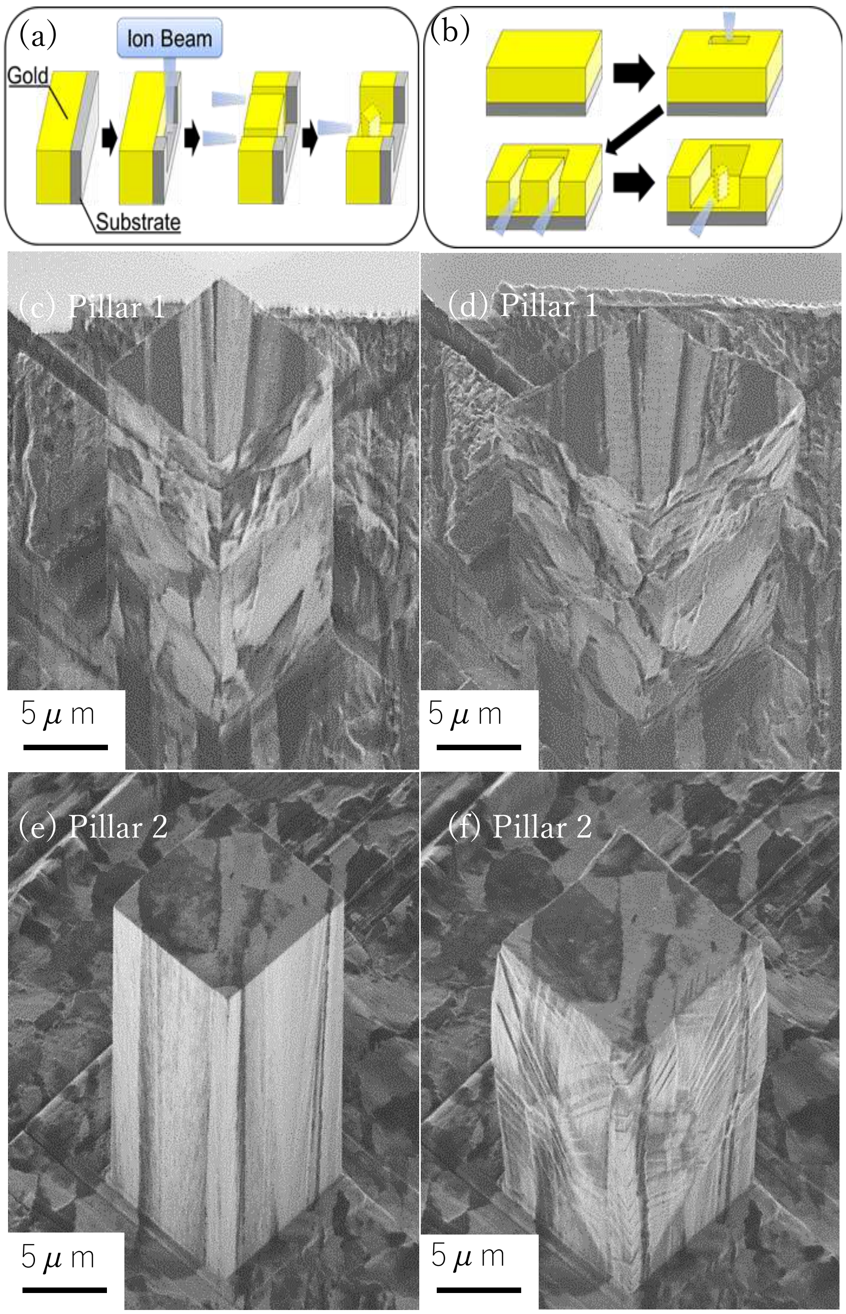

Figure 9. Schematic views of (a) pillar 1 and (b) pillar 2. SIM images of (c) (d) pillar 1 and (e) (f) pillar 2 before and after compression test.

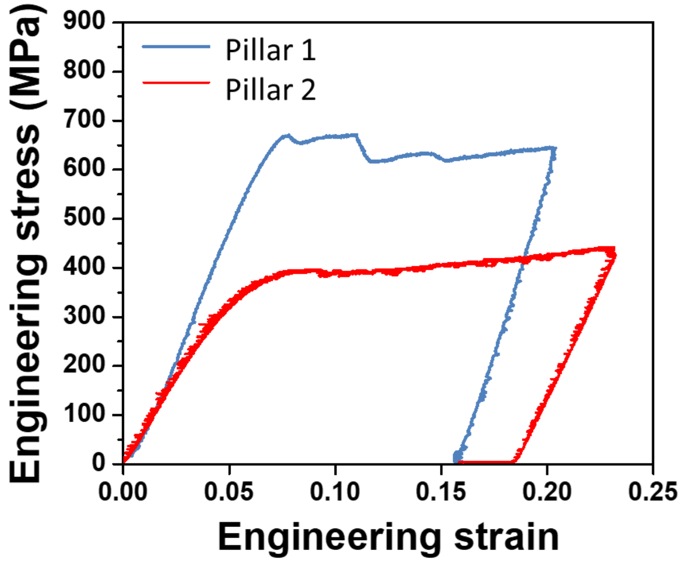

Figure 10. Engineering stress-strain curves.

pillar 1. In contrast, deformation with slip lines was observed in pillar 2, and it was generally defined as multiple slip deformation (34). Figure 10 shows the engineering stress-strain curves. Load drops and non-continuous change of the slope were observed in the plastic region for pillar 1, while the slope remained almost constant in the plastic region for pillar 2. Considering the deformation behavior of pillar 1, the load drop and the change in the slope are attributed to the brittle fracture. Pillar 1 showed a higher σ_Y (ca. 650MPa) than that of pillar 2 (ca. 300MPa). These anisotropies in the deformation behavior and the σ_Y can be explained by the information obtained from the microstructure analysis. The XRD pattern showed typical result of FCC Au and strong intensity for the peak of [200] orientation, shown in Fig. 11(a). Grain size of the Au film was estimated using the XRD result and the Scherrer equation. The grain size was estimated to be 14.7nm. From EBSD mapping with respect to the transverse direction (TD, Fig. 11(b)), the normal direction (ND, Fig. 11(c)), and the reference direction (RD, Fig. 11(d)), the Au film was confirmed to be composed of columnar grains, where the long-axis is parallel to growth direction of the Au film, and all grains showed [001] direction. This orientation is consistent with the XRD result, which the dominant peak is the peak of [200] orientation. On the hand, the grain size calculated from the EBSD mapping images was about 1.34µm, which is much larger than the value obtained from the Scherrer equation. The difference observed in the grain size was further clarified through TEM observation. As shown in Fig. 11(e), columnar grains were observed. Width of the grains is ca. 16~40nm, which corresponds well with the grain size calculated using the Scherrer equation. From the XRD, the EBSD mapping, and the TEM results, we can summarize that the Au film is composed of columnar textures with an average width of 1.34µm, and each texture is composed of columnar grains having an average width at about several tens of nanometer. In addition, the micro-columnar textures and the nano-columnar grains have the same crystal orientation, and the grain-like microstructures observed in EBSD mapping are confirmed to be textures. The anisotropy observed in the deformation behavior and the σ_Y can be explained from the columnar microstructures. For pillar 2, multiple slip deformation often occurs when FCC single crystal was compressed along [100] direction (34). Grains of the Au film are oriented in [100] direction. The grains in pillar 2 were compressed along the long-axis, which is the [100] direction. This led to formation of the slip lines shown in Fig. 9(f). Regarding the difference in the σ_Y, for pillar 1, the compression direction is perpendicular to the long-axis of the nanograins, which are orientated in [100] direction. Hence the compression can be treated as compression of grains with random orientation. In contrast, pillar 2 was compressed along [100] direction. In this compression direction, the compression can be deemed as compression of assemblies of columnar single crystals having the same crystal orientation. Because of the difference in the compression conditions, the relationship between critical resolved shear stress τ_{CRSS} and σ_Y is different for pillar 1 and 2. For compression of randomly oriented crystals (pillar 1), the relationship is represented by the Taylor model (35):

$$\sigma_{Y,Pillar\ 1} = M\tau_{CRSS} \ , \qquad [3]$$

where, M is the Taylor factor, and the value is about 3.1 for FCC metal. For compression of assemblies of single crystals (pillar 2), the relationship is represented by the Schmid model [36]:

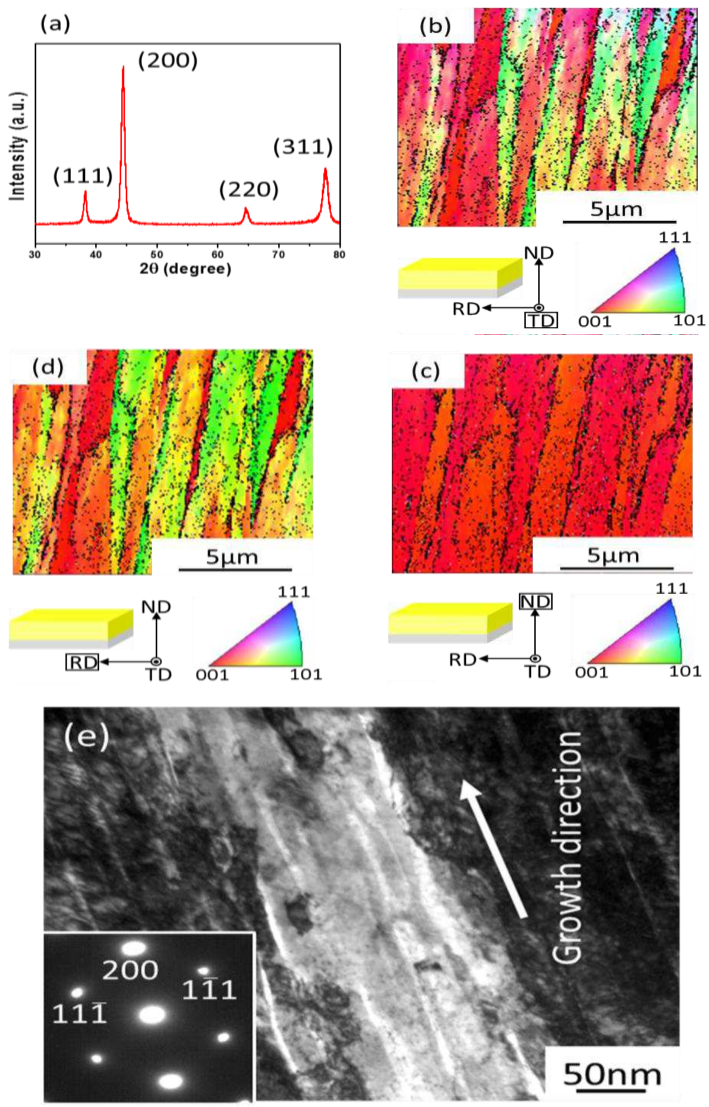

Figure 11. (a) XRD pattern and EBSD mapping coresponds to the (b) TD, (c) ND, and (d) RD, and (e) bright field TEM image of Au film.

$$\sigma_{Y,Pillar\ 2} = \frac{\tau_{CRSS}}{\cos\theta\cos\varphi}\ , \qquad [4]$$

where, $\cos\theta\cos\varphi$ is the Schmid's factor. The Schmid's factor for single crystals deformed along [100] direction is 0.408. Ratio of the σ_Y's ($\sigma_{Y,Pillar\ 1}/\sigma_{Y,Pillar\ 2}$) obtained from eqs. [3] and [4] is 1.26, which shows the estimated σ_Y of pillar 1 is higher than the σ_Y of pillar 2. This is consistent with the σ_Y's obtained from the stress-strain curves, the σ_Y of pillar 1 is 650MPa and the σ_Y of pillar 2 is 300MPa. On the other hand, ratio of the σ_Y's obtained from stress-strain curves is about 2.16. The difference in the ratio might be attributed to the texture boundary. The texture boundary is expected to affect the strength similar to the grain boundary (37).

Average width of the textures is 1.34μm, and dimensions of the micro-pillar are $10\times10\times20\ \mu m^3$. This implies that pillar 1 would contain more number of textures and of course larger texture boundary area than that in pillar 2. Therefore, the texture boundaries contributed to the strengthening and resulted higher ratio of the σ_Y's.

Early-Stage Diagnosis of Parkinson's Disease

This chapter describes the validity of applying the MEMS accelerometer to the diagnosis of Parkinson's disease.

Background

Analysis of abnormal gait can provide important information about diseases and injuries. For example, patients with Parkinson's disease (PD) often exhibit shuffling, festinating, and freezing of gait. The most widely used clinical rating scale for PD, the Unified Parkinson's Disease Rating Scale, includes observation of gait (38). Patients with cerebellar disorders sometimes have a wide-based (atactic) gait, and those with cerebral vascular disease sometimes exhibit a hemiplegic gait. Recent articles have reported changes in gait, such as reduced gait velocity and stride length, in diseases with gait disorders and in other conditions, such as Alzheimer's disease (39) and depression (40).

Clinical gait analysis is performed mostly by health-care providers using visual observation (41). Although this method is the most readily accessible means of gait analysis available to health-care providers (42), it is a subjective and qualitative method that is inadequate for assessing changes in gait features during ongoing treatment interventions. It is also difficult for clinicians to share this information with health-care providers and patients. Motion capture systems are used in clinical research for gait analysis (43) and scientific research (44). Because they provide well-quantified and accurate results, these systems are currently considered to be the criterion standard for clinical gait analysis (45). While the special equipment needed for motion capture is expensive and requires a large space, few medical institutions can use these systems for clinical gait analysis (42).

Several studies have proposed gait analysis methods using inertial measurement units (IMUs) to solve the problems (46-50). IMUs used in these methods are inexpensive and wearable (51). In particular, we focused on methods that estimate trajectories of a foot because such methods can be used to obtain several spatial gait parameters. Sabatini et al. proposed an IMU-based gait analysis method that estimates a two-dimensional trajectory in the sagittal plane of a foot during walking (46). Other studies have proposed gait analysis methods that estimate the three-dimensional foot trajectory during walking in a stepwise manner to obtain values of foot clearance (48, 50, 52). The trajectory estimation methods reported in several studies (46, 50, 52-54) use an IMU attached on the dorsum of the foot and are better for obtaining this gait feature. As described above, and to the knowledge of the authors, there is no report of a method that estimates three-dimensional foot trajectory from an IMU attached on the shank during waking in a stepwise manner to calculate simultaneously spatial and temporal clinical gait parameters, including stride length, gait speed, stride duration, stance duration and swing duration.

In this study, we demonstrate the validity of the proposed giant analysis method using MEMS accelerometer while comparing the motion capture analysis.

Experimental

Our proposed gait analysis system is illustrated in Fig. 11(a). For gait analysis, we used two IMUs (TSND121, ATR-Promotions, Kyoto, Japan; Fig. 11(b)) with a triaxial accelerometer (±8G range), triaxial gyroscope (±1000° per range), and Android OS tablet (ZenPad10, ASUSTeK Computer Inc., Taipei, Taiwan; Fig. 11(c)). Raw accelerometer and gyroscope signals were sampled at 100Hz (16 bits per sample). The size of the IMU is 37mm×46mm×12 mm and its weight is about 22g. IMUs are attached on the shanks (just above the ankles) with bands as shown in Fig 11(b). The inertial coordinate system used to represent foot orientation and position is also shown in Fig. 11(b). Acceleration and angular velocity data of both the shanks measured during walking are transmitted to the tablet through Bluetooth.

We conducted an experimental evaluation of our proposed method to validate the

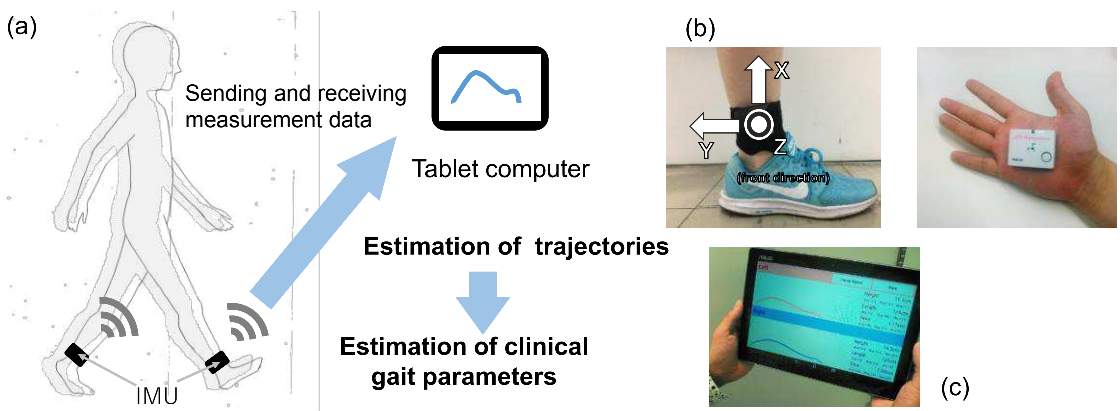

Figure 11. The proposed gait analysis system.

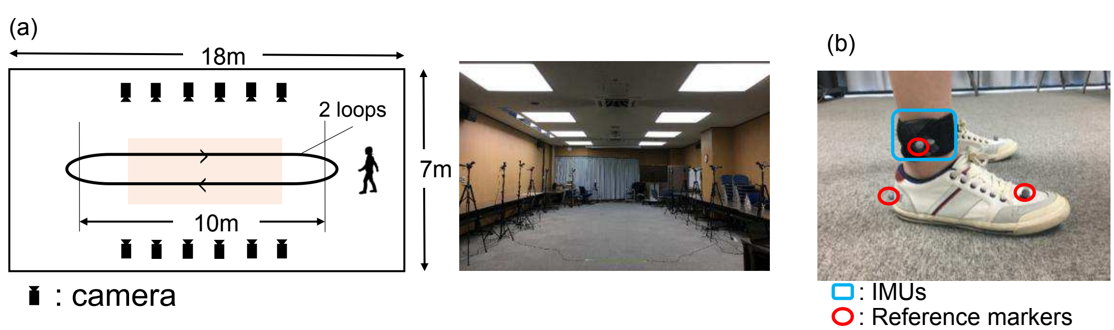

Figure 12. Motion capture system.

accuracy of the trajectory estimation of the shanks (just above the ankles) to verify whether it allows the analysis of gait for clinical purposes. Twenty healthy people participated in the experiment, and we used a motion capture system as the criterion standard for the evaluating gait in a clinical setting. We evaluated the accuracy of our proposed method for calculating the estimated trajectory and clinical gait parameters. We used an IMU attached on the shanks for the experimental evaluation.

An optical motion capture system (Nobby Tech. Ltd., Tokyo, Japan) was used as the reference system. We used 12 cameras, and the motion capture volume was about 2m ±7m ±1m (width, length, and height) as shown in Fig. 12(a). The position error of the markers of the motion capture system during the calibration was less than 1mm. The dimensions of the floor of the room were 18m ±7m (length and width) as shown in Fig. 12(a). Three optical markers were attached on each foot as shown in Fig. 12(b). Two of the three markers were attached on the heel and the toe (metatarsal head II) to assess gait parameters. The third marker was attached on the IMU to evaluate the trajectory estimation. To synchronize the IMU and the motion capture system, the participants hit their heel to the floor before the gait measurement. The peaks of the spike waveforms, that were caused by the heel hits of the participants, in both the IMU signals and the motion capture system data were used to define time 0. We recruited 20 able-bodied volunteer participants, with no history of gait abnormalities, from the Tokyo Institute of Technology for the experimental evaluation. The Ethics Committee of Tokyo Institute of Technology approved the protocols for the evaluation, and all participants provided their written informed consent. Because of technical problems with the motion capture system, the data for one of the 20 volunteer participants were excluded from the analyses. Ultimately, we used data from 19 participants (mean age 23.9 years, 9 men and 10 women, mean height 1.66±0.07m and mean body mass index 20.2±2.7).

As an example of the application of the proposed method to PD patients, we used the method to analyze gait in one healthy elderly participant and four patients with PD. The healthy elderly participant was recruited from a public interest incorporated association in Machida City, Tokyo that provides human resource services for elderly people. Patients with PD were recruited from Kanto Central Hospital, Tokyo. PD had been diagnosed by a physician. The exclusion criteria for this study were past history of other neurological or orthopedic disorders that can affect gait or posture (excluding PD). The healthy elderly participant and the four PD participants provided written informed consent in accordance with requirements of the Ethics Committee of Tokyo Institute of Technology. The Kanto Central Hospital Ethics Committee and the Ethics Committee of Tokyo Institute of Technology approved the protocol for the application of the proposed method.

To construct the spike waveforms for synchronization between the IMU and the motion capture system, the participants hit their heel to the floor before the gait measurement. In two trials, the participants walked on a flat floor at their own self-selected natural pace and a slow pace. In each trial, the participants walk straight in the motion capture volume and turned outside of the motion capture volume. Thus, each trial comprised four straight walks (two round trips; Fig. 12(a)). We used the gait data obtained as the participants walked in the motion capture volume and removed the gait data as the participants turned outside of the motion capture volume.

To consider the validity of the estimation of foot trajectory from IMUs attached on the shanks, we calculated correlations between stride length estimated with the proposed method, measured with a motion capture marker attached on the IMU, and measured with a motion capture marker attached on the heel.

Results & Discussion

To evaluate the proposed method, the shank (just above the ankle) trajectory and clinical gait parameters calculated by our proposed method were compared with those collected by the motion capture system. The comparisons of trajectory information were conducted in the sagittal plane. Five clinical gait parameters of (1) stride length, (2) gait speed, (3) stride duration, (4) stance duration, and (5) swing duration were compared.

The trajectories of our proposed method and the reference data are shown in Fig. 13. The R value between displacement in the direction of forward movement calculated with the proposed method and measured with a marker attached on the IMU was 0.978 as shown in Fig. 14(a). The R value between the maximum vertical displacement calculated with the proposed method and measured with a marker attached on the IMU was 0.925 as shown in Fig. 14(b). The R value between displacement in the direction of forward movement calculated with the marker attached on the IMU and that measured with the marker attached on the heel was 0.994 as shown in Fig. 14(c). Figure 15 shows the agreement between the proposed method and the motion capture system in Bland–Altman plots. The mean±1 SD accuracy of stride length was 0.054±0.031m as shown in Fig. 15(a). The R value between displacement in the direction of forward movement calculated with the proposed method and measured with a marker attached on the heel was 0.978 (Fig. 15(a)). The mean ±1 SD accuracy were as follows: 0.034±0.039m/s for gait speed (Fig. 15(b)); 0.002±0.020s for stride duration (Fig. 15(c); 0.000±0.017s for stance duration (Fig. 15(d)); and 0.002±0.024s for swing duration (Fig. 15(e)). The shank trajectory over 15 steps for each participant is shown in Fig. 16.

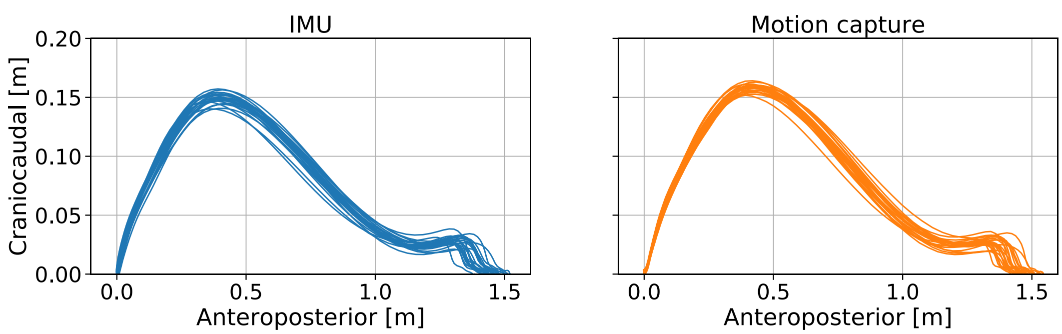

Figure 13. Comparison of Accelerometer and motion capture.

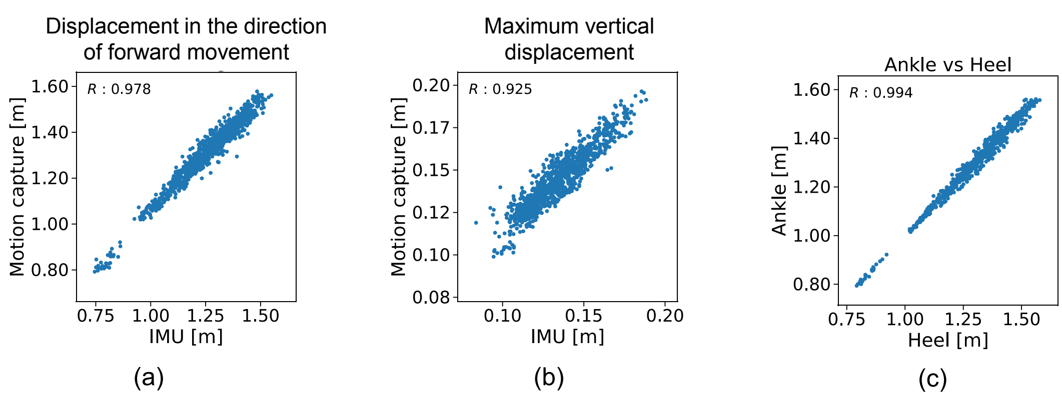

Figure 14. The trajectories of our proposed method and the reference data.

We have proposed a new method for gait analysis that uses IMUs attached on the shanks to estimate foot trajectory and then to obtain estimated clinical gait parameters. The gait parameters obtained with the proposed method consists of stride length, gait speed, stride duration, stance duration, and swing duration. The experimental results show that the proposed method can be used to calculate clinical gait parameters by estimating foot trajectory. The proposed gait analysis method comprises two IMUs with a tri-axial accelerometer, tri-axial gyroscope, and tablet computer. This method can be applied in a variety of locations outside of the gait laboratory and is less expensive than conventional gait analysis methods such as motion capture systems. The clinical advantage is that the patient burden is low because of the light weight (about 24g) and easy attachment of the

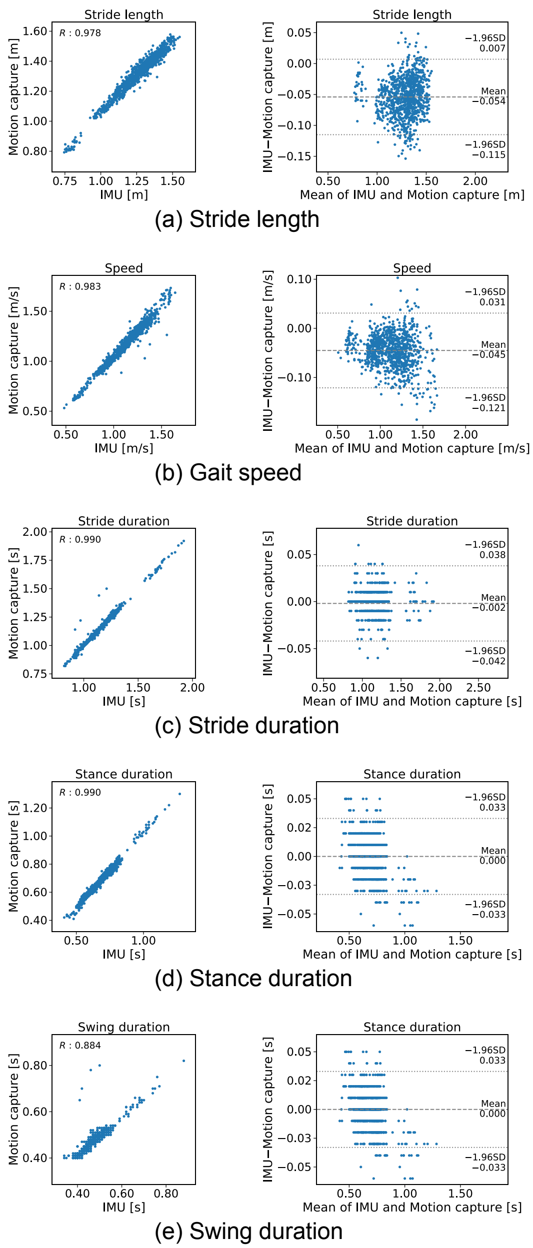

Figure 15. The R value between displacement in the direction of forward movement.

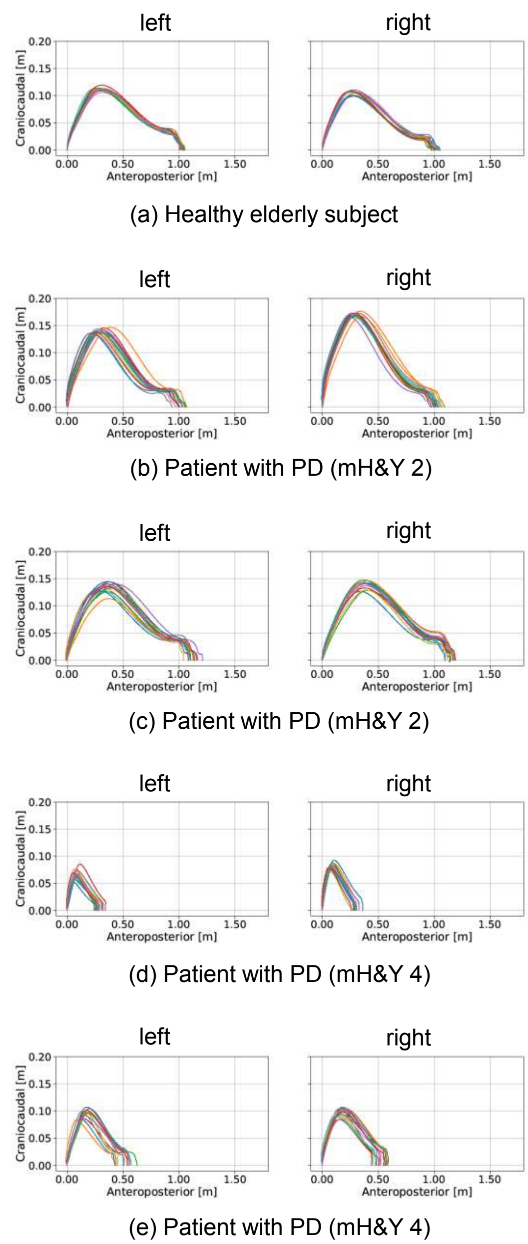

Figure 16. The proposed method and the motion capture system.

IMUs. We therefore anticipate that the proposed method would be suitable for clinical gait analysis. As for the location of the IMUs, the R value between displacement in the direction of forward movement as measured with the marker attached on the IMU and as measured with the marker attached on the heel (0.994) indicates that the location of the IMUs is valid at least for estimating the stride length. The R value between displacement in the direction of forward movement as estimated by the proposed method and as measured with the marker of the motion capture system attached on the IMU indicates that displacement in the direction of forward movement estimated by the proposed method explained 96% of the variation in displacement in the direction of forward movement as measured with the motion capture system.

The mean error of stride length estimated with the proposed method was 0.054±0.031m. This result suggests that the proposed method can estimate clinical gait parameters such as stride length. A previous method in which the location of IMU is on the dorsum of a foot found that the mean accuracy±precision was 0.015±0.068m (48). The IMU location on the shank may cause bias of this order of accuracy. We expected that further development of the method will overcome this limitation of performance. Several studies (55, 56) have found that stride length is shorter in patients with PD than it is in healthy controls as observed in the example of the application of the proposed method. For example, Morris et al. (57) reported that stride length in PD patients in the off state was 0.96±0.19m, which was shorter than the stride length of 1.46±0.08m as measured in healthy age-matched controls. The R value between displacement in the direction of forward movement estimated by the proposed method and measured with the marker of the motion capture system attached on the heel indicates that stride length estimated by the proposed method explained 96% of the variation measured with the motion capture system. This result suggests that IMUs are potentially useful in clinical gait analysis. We expect further development of the proposed method to evaluate the gait in people with PD.

Summary

We proposed and demonstrated a gold proof-mass MEMS accelerometer for micro-G level sensing. The multi-layer structure of both proof mass and spring can be achieved by the multi-layer metal technology so that B_N can be reduced. The measurement results of the developed MEMS devices were consistent with the design values. The B_N was experimentally obtained to be 22nG/√Hz. The evaluation results confirmed that the proposed MEMS device has potential for micro-G level sensing.

Next, the electroplated Au film was confirmed to be composed of nano-columnar grains embedded in micro-columnar textures. Brittle fracture was observed in the micro-pillar having the long-side perpendicular to the long-axes of the columnar microstructures. Typical multiple slip deformation observed in polycrystalline specimens was observed in the micro-pillar having the long-side parallel to the long-axes. The σ_Y of pillar 1 was roughly two times higher than that of pillar 2. The differences in the deformation behavior and the σ_Y are suggested to be caused by the differences in the compression direction and the total texture boundary area in each pillar.

Finally, our results suggest that the proposed method is suitable for gait analysis whereas there is room for improvement of its accuracy. Unlike methods that use motion capture systems, this method can be used in a variety of locations, such as in the corridor of a medical center. Further development of our proposed method is expected to enable clinicians to share objective information about gait features with health-care providers and patients.

In conclusion, these results of experiments regarding the sensor, the material and the diagnosis suggest that our microgravity sensor can pave the way for the early-stage diagnosis of Parkinson's disease.

Acknowledgments

This work was supported by JST CREST Grant Number JPMJCR1433, Japan.

References

1. D. K. Shaeffer, IEEE Commun. Mag., **51** 100 (2013).
2. J. Laine and D. Mougenot, Proc. TRANSDUCERS 2007 (2007 Int. Solid-State Sensors, Actuators and Microsystems Conf.), 1473 (2007)
3. G. Krishnan, C. U. Kshirsagar, G. K. Ananthasuresh, and N. Bhat, J. Indian Inst. Sci., **87**, 333 (2007).
4. S. Scudero, A. D'Alessandro, L. Greco, and G. Vitale, Proc. 2018 IEEE Int. Conf. on Environmental Engineering (2018), (DOI: 10.1109/EE1.2018.8385252)
5. M. Lemkin and B. E. Boser, IEEE J. Solid-State Circuits, **34**, 456 (1999).
6. B. V. Amini and F. Ayazi, J. Micromech. Microeng., **15,** 2113 (2005).
7. H. Kulah, J. Chae, N. Yazdi, and K. Najafi, IEEE J. Solid-State Circuits, **41,** 352 (2006).
8. B. E. Boser and R. T. Howe, IEEE J. Solid-State Circuits, **31**, 366 (1996).
9. N. Yazdi, K. Najafi, and A. S. Salian, J. Microelectromech. Syst., **12,** 476 (2003).
10. K.-H. Han and Y.-H. Cho, J. Microelectromech. Syst., **12,** 11 (2003).
11. J. Chae, H. Kulah, and K. Najafi, J. Microelectromech. Syst., **14,** 235 (2005).
12. B. V. Amini, R. Abdolvand, and F. Ayazi, IEEE J. Solid-State Circuits, **41**, 2983 (2006).
13. R. Abdolvand, B. V. Amini, and F. Ayazi, J. Microelectromech. Syst., **16**, 1036 (2007).
14. H. Qu, D. Fang, and H. Xie, IEEE Sensors Journal, **8**, 1511 (2008).
15. Y. Dong, P. Zwahlen, A.-M. Nguyen, F. Rudolf, and J.-M. Stauffer, Proc. IEEE/ION Position, Location and Navigation Symposium, 32 (2010).
16. B. Homeijer, D. Lazaroff, D. Milligan, R. Alley, J. Wu, M. Szepesi, B. Bicknell, Z. Zhang, R. G. Walmsley, and P. G. Hartwell, Proc. 2011 IEEE 24th International Conference on Micro Electro Mechanical Systems, 585 (2011).
17. W. Zhu, Y. Zhang, G. Meng, C. S. Wallace, and N. Yazdi, Proc. 2016 IEEE 29th International Conference on Micro Electro Mechanical Systems, 926 (2016).
18. J. Wu, G. K. Fedder, and L. R. Carley, IEEE J. Solid-State Circuits **39**, 722 (2004).
19. S. S. Tan, C. Y. Liu, L. K. Yeh, Y. H. Chiu, M. S.C. Lu, and K. Y. J. Hsu, IEEE Trans. Circuit Syst. I, **58**, 2661 (2011).
20. M.-H. Tsai, Y.-C. Liu, K.-C. Liang, and W. Fang, J. Microelectromech. Syst., **24**, 1916 (2015).

21. T. Konishi, D. Yamane, T. Matsushima, G. Motohashi, K. Kagaya, H. Ito, N. Ishihara, H. Toshiyoshi, K. Machida, and K. Masu, Jpn. J. Appl. Phys., **52**, 06GL04 (2013).
22. D. Yamane, T. Konishi, T. Matsushima, K. Machida, H. Toshiyoshi, and K. Masu, Appl. Phys. Lett., **104**, 074102 (2014) .
23. D. Yamane, T. Konishi, T. Safu, Hiroyuki Ito, H. Toshiyohi, K. Masu, and K. Machida, Proc. Asia-Pacific Conference of Transducers and Micro-Nano Technology (APCOT 2016), Kanazawa, Japan, June 26-29, 299 (2016).
24. D. Yamane, T. Konishi, T. Safu, H. Toshiyoshi, M. Sone, K. Machida, H. Ito, and Kazuya Masu, Sensors and Materials, **31**, 2883 (2019).
25. K. Machida, S. Shigematsu, H. Morimura, Y. Tanabe, N. Sato, N. Shimoyama, T.Kumazaki, K. Kudou, M. Yano, and H. Kyuragi, IEEE Trans. Electron Devices, **48**, 2273 (2001).
26. D. R. Lide, CRC Handbook of Chemistry and Physics (CRC Press, Boca Raton, FL, 1994) 75th ed.
27. W. Yun, R. T. Howe, and P. R. Gray, Proc. Technical Digest IEEE Solid-State Sensor and Actuator Workshop, 126 (1992).
28. J. H. Smith, S. Montague, J. J. Sniegowski, J. R. Murray, and P. J. McWhorter, Proc. International Electron Devices Meeting, 609 (1995).
29. M.-H. Tsai, Y.-C. Liu, and W. Fang, J. Microelectromech. Syst., **21**, 1329 (2012).
30. C. Lu, M. Lemkin, and B. E. Boser, IEEE J. Solid-State Circuits, **30**, 1367 (1995).
31. M. A. Lemkin, B. E. Boser, D. Auslander, and J. H. Smith, Proc. International Solid State Sensors and Actuators Conference (Transducers '97), 1185 (1997).
32. N. Yazdi and K. Najafi, 1999 IEEE International Solid-State Circuits Conference. Digest of Technical Papers. ISSCC. First Edition (Cat. No.99CH36278), 132 (1999).
33. M. Yoshiba, C.-Y. Chen, T.-F.M. Chang, T. Nagoshi, D. Yamane, K. Machida, K. Masu, M. Sone, Mater. Trans., **57**, 1257 (2016).
34. J.R. Greer, W.C. Oliver, W.D. Nix, Acta Mater., **53**, 1821 (2005).
35. G.I. Taylor, J. Inst. Metal, **62**, 307 (1938).
36. E. Schmid, W. Boas, Plasticity of Crystals (Hughes, London, 1950).
37. N. J. Petch, J. Iron, Steel Inst., **174**, 25 (1953).
38. C. G. Goetz, B. C. Tilley, S. R. Shaftman, G.T. Stebbins, S. Fahn, P. Martinez-Martin, W. Poewe, C. Sampaio, M. B. Stern, R. Dodel, B. Dubois, R. Holloway, J. Jankovic, L. Kulisevsky, A. E. Lang, A. Lees, S. Leurgans, P. A. Lewitt, D. Nyenhuis, C. W. Olanow, O. Rascol, A. Schrag, J. A. Teresi, J.J. Van Hilten, N. Lapelle, Movement Disorder Society, U.R.T.F. Mov. Disord., **23**, 2129 (2008).
39. M.M. Mielke, R.O. Roberts, R. Savica, R. Cha, D.I. Drubach, T. Christianson, V. S. Pankratz, Y. E. Geda, M. M. Machulda, R. J. Ivnik, D. S. Knopman, B. F. Boeve, W. A. Rocca, and R. C. Petersen, J. Gerontol. A Biol. Sci. Med. Sci., **68**, 929 (2013).
40. M. R. Lemke, T. Wendorff, B. Mieth, K. Buhl, and M. Linnemann, J. Psychiatr. Res., **34**, 277 (2000).
41. D. E. Krebs, J. E. Edelstein, and S. Fishman, Phys. Ther., **65**, 1027 (1985).
42. S. Barker, R. Craik, W. Freedman, N. Herrmann, and H. Hillstrom, Med. Eng. Phys., **28**, 460 (2006).
43. J. L. Mcginley, R. Baker, R. Wolfe, and M. E. Morris, Gait Posture, **29**, 360 (2009).

44. D. E. Lieberman, M. Venkadesan, W. A. Werbel, A. I. Daoud, S. D'andrea, I. S. Davis, R. O. Mang'eni, and Y. Pitsiladis, Nature, **463**, 531 (2010).
45. M. H. Cameron and J. M. Wagner, Curr. Neurol. Neurosci. Rep., **11**, 507 (2011).
46. M. Sabatini, C. Martelloni, S. Scapellato, and F. Cavallo, IEEE Trans. Biomed. Eng., **52**, 486 (2005).
47. S. T. Moore, H. G. MacDougall, J. M. Gracies, H. S. Cohen, and W. G. Ondo, Gait Posture, **26**, 200 (2007).
48. B. Mariani, C. Hoskovec, S. Rochat, C. Bula, J. Penders, and K. Aminian, J. Biomech., **43**, 2999 (2010).
49. J. R. Rebula, L. V. Ojeda, P. G. Adamczyk, and A. D. Kuo, Gait Posture, **38**, 974 (2013).
50. N. Kitagawa and N. Ogihara, Gait Posture, **45**, 110 (2016).
51. Y. Fujiki, P. Tsiamyrtzis, and I. Pavlidis, CHI'09 Extended Abstracts on Human Factors in Computing Systems, Boston, MA, USA, 3425 (2009).
52. B. Mariani, S. Rochat, C. J. Bula, and K. Aminian, IEEE Trans. Biomed. Eng., **59**, 3162 (2012).
53. Salarian, H. Russmann, F. J. Vingerhoets, C. Dehollain, Y. Blanc, P. R. Burkhard, and K. Aminian, IEEE Trans. Biomed. Eng., **51**, 1434 (2004).
54. Tunca, N. Pehlivan, N. Ak, B. Arnrich, G. Salur, and C. Ersoy, Sensors (Basel), **17**, 825 (2017).
55. H. Stolze, J. P. Kuhtz-Buschbeck, H. Drucke, K. Johnk, M. Illert, and G. Deuschl, J. Neurol. Neurosurg. Psychiatry, **70**, 289 (2001).
56. C. Curtze, J. G. Nutt, P. Carlson-Kuhta, M. Mancini, and F.B. Horak, Mov. Disord., **30**, 1361 (2015).
57. M. Morris, R. Iansek, J. Mcginley, T. Matyas, and F. Huxham, Mov. Disord., **20**, 40 (2005).